FULL PAPER

Magnetic Resonance in Medicine 000:000–000 (2012)

In Vivo Free Induction Decay Based 3D Multivoxel Longitudinal Hadamard Spectroscopic Imaging in the Human Brain at 3 T

Assaf Tal,[1]* Gadi Goelman,[1,2] and Oded Gonen[1]

We propose and demonstrate a full 3D longitudinal Hadamard spectroscopic imaging scheme for obtaining chemical shift maps, using adiabatic inversion pulses to encode the spins' positions. The approach offers several advantages over conventional Fourier-based encoding methods, including a localized point spread function; no aliasing, allowing for volumes of interest smaller than the object being imaged; an option for acquiring noncontiguous voxels; and inherent outer volume rejection. The latter allows for doing away with conventional outer volume suppression schemes, such as point resolved spectroscopy (PRESS) and stimulated echo acquisition mode (STEAM), and acquiring non-spin-echo spectra with short acquisition delay times, limited only by the excitation pulse's duration. This, in turn, minimizes T_2 decay, maximizes the signal-to-noise ratio, and reduces J-coupling induced signal decay. Results are presented for both a phantom and an in vivo healthy volunteer at 3 T. Magn Reson Med 000:000–000, 2012.

Key words: longitudinal Hadamard; spectroscopic imaging; CSI

In vivo proton (^{1}H) magnetic resonance spectroscopy, with suppression of the dominant signals from water and extracranial fat, provides information about small metabolite molecules, including amino acids and lipids in the brain (1–4). Multivoxel MR spectroscopic imaging (MRSI) is conventionally carried out using gradient Fourier-encoded chemical-shift-imaging (CSI) (5,6). The inherent low signal-to-noise ratio (SNR) of in vivo MRSI dictates voxel volumes on the order of 1 cm^3 in humans, much larger than the typical ~1 mm^3 voxels associated with MRI. At such low spatial resolutions, the sinc-shaped point spread function (PSF) of Fourier encoding is particularly diffuse, leading to an inherent SNR loss (7), as well as intervoxel localization errors and outer-volume contamination with signals from outside the volume of interest (VOI), also known as "voxel bleed" (8–10). Spatially filtering the data at the postprocessing stage can reduce localization errors at the cost of widening the voxel and decreasing the SNR per unit volume (11); filtering can also be applied in the acquisition stage without reducing the SNR per unit volume, but at the cost of multiple averages and voxel-widening (12).

Particularly troublesome are the intense water and lipid resonances residing outside the VOI. Their suppression is vital to obtaining good quality spectra and requires combining outer volume suppression (OVS) with selective excitation, achieved with variants of stimulated echo acquisition mode (STEAM) or point resolved spectroscopy (PRESS) (13,14). These echo-based localization modules are also crucial for eliminating aliasing artifacts in fields-of-view (FOV) smaller than the head, but require an echo delay, echo time (TE), that leads to T_2 signal losses and J-coupling modulation. Furthermore, the use of refocusing pulses in PRESS leads to inherently low pulse bandwidths per unit specific absorption rate (SAR) and pronounced chemical shift displacements at the VOI's edges, while the more robust STEAM reduces the available SNR twofold.

In this article, we propose a non-spin-echo 3D MRSI technique based on longitudinal Hadamard encoding (longitudinal Hadamard spectroscopic imaging, L-HSI). Its PSF is determined only by the sharpness of the radiofrequency (RF) inversion profile and can be made highly localized, eliminating CSI's voxel bleed artifacts. This bleed reduction, especially from far-away voxels, combined with the longitudinal nature of the encoding and inherent addition–subtraction reconstruction scheme used (which rejects signals from outside the VOI), allows one to omit the standard OVS modules. To remove residual lipid signals, a simpler module, which spatially excites and dephases the cranial lipids, can be inserted in between encoding and excitation, with only a modest reduction in the metabolites' signal due to their long T_1 relaxation times (e.g., for $T_1 \sim 1.4$ s and a 20 ms RF lipid suppression module, a signal reduction of only $1 - e^{-20/1400} \approx 1.4\%$ will be incurred). This, in turn, facilitates the acquisition of non-spin-echo spectra. Hadamard encoding does not suffer from aliasing, and thus the FOV and VOI are always the same size and can be chosen smaller than the object imaged. The VOI itself does not need to be contiguous, allowing simultaneous coverage of disjoint regions without incurring the overhead of having to sample the space in between. Finally, the adiabatic inversion RF pulses render the method insensitive to volume and surface-coil B_1 inhomogeneity on transmit. While several of these advantages were exploited previously to different extents, in both imaging and spectroscopy, often by Hadamard encoding just a subset of all available dimensions (15–21), their

[1]Department of Radiology, NYU School of Medicine, New York, New York, USA.

[2]MRI Laboratory, Human Biology Research Center, Department of Medical Biophysics, Hadassah Hebrew University Medical Center, Jerusalem, Israel.

Grant sponsor: NIH; Grant numbers: EB01015 and NS050520; Grant sponsor: Human Frontiers Science Project

*Correspondence to: Assaf Tal, Ph.D., Department of Radiology, NYU School of Medicine, 660 1st Avenue, 4th Floor, New York, NY 10016. E-mail: assaf.tal@nyumc.org

Received 5 January 2012; revised 14 April 2012; accepted 17 April 2012.

DOI 10.1002/mrm.24327

Published online in Wiley Online Library (wileyonlinelibrary.com).

comprehensive 3D ^{1}H-MRSI approach is now demonstrated with computer simulations, in a phantom and in the brain of a volunteer at 3 T.

THEORY

L-HSI spatially encodes the magnetization in the VOI along a given direction either parallel, $M_z \rightarrow M_z$, or antiparallel, $M_z \rightarrow -M_z$ to the external magnetic field, B_0, according to the +1 s and −1 s of the ith row of an Nth-order Hadamard matrix, $\mathbf{H}$ (18). This is repeated for each of the N rows of $\mathbf{H}$, with shaped pulses under a gradient (22,23). An Nth-order Hadamard matrix, $\mathbf{H}$, is an $N \times N$ array whose elements are ± 1 and is its own transpose and inverse, $\mathbf{H}^{-1} = \mathbf{H}^{\mathrm{T}} = N \cdot \mathbf{H}$:

$$\sum_{k=1}^{N} H_{ik} H_{kj} = N\delta_{ij}. \quad [1]$$

Hadamard matrices of order $4k$ can be constructed for any positive integer k (24).

The theory of Hadamard encoding is most easily illustrated in one dimension. Let M_i be the equilibrium longitudinal magnetization in the ith voxel ($i = 1,\ldots,N$), that contains, without loss of generality, a single chemical species with a singlet resonating at Ω_0. Selective excitation of that voxel, followed immediately by acquisition, would yield a signal $s_i^{(\mathrm{single})}(t) = M_i e^{i\Omega_0 t}$. In longitudinal Hadamard encoding, N experiments are carried out: in the jth experiment, a multiband inversion pulse is applied that inverts the magnetization in the ith voxel ($i = 1,\ldots,N$) if $H_{ij} = -1$. The pulse's effect on each voxel's longitudinal equilibrium magnetization can be modeled as $M_i \overset{i\text{th experiment}}{\longrightarrow} H_{ij} M_i$. The spins are then excited onto the xy plane and a signal:

$$S_j(t) = \sum_{p=1}^{N} H_{pj} M_p e^{i\Omega_0 t} = \sum_{p=1}^{N} H_{pj} s_p^{(\mathrm{single})}(t) \qquad j = 1, l \ldots, N, \quad (2)$$

is acquired from all voxels simultaneously.

To recover the free induction decay (FID) from the kth voxel, an inverse Hadamard transform is applied, in which the acquired signals $S_j(t)$ ($j = 1,..,N$) are summed with weighting factors given by the rows of an Nth-order Hadamard matrix:

$$\sum_{j=1}^{N} H_{kj} S_j = \sum_{j=1}^{N} H_{kj} \sum_{k=1}^{N} H_{pj} s_p^{(\mathrm{single})}(t) = s_k^{(\mathrm{single})}(t) \quad [3]$$

where the orthogonality of two Hadamard matrices (Eq. 1) is used. Fourth-order Hadamard encoding (i.e., $N = 4$) in 1D is illustrated in Fig. 1a: four acquisitions are carried out, yielding signals S_1, S_2, S_3, and S_4. Figure 1b shows the decoding process (Eq. 3), in which the four linear combinations $\Sigma_{j=1}^{4} H_{kj} S_j$ ($k = 1,2,3,4$) are formed, with the kth combination recovering the signal from the kth voxel.

The one-dimensional encoding scheme can be extended to three dimensions by applying three Hadamard pulses consecutively, each in the presence of a gradient along a different orthogonal axis that we shall arbitrarily term x, y, and z. Consider a volume containing $N_x \times N_y \times N_z$ voxels (each N_i being a Hadamard order). The voxels need not be spatially contiguous, as the RF inversion pulses need not irradiate spatially contiguous bands. Let M_{ijk} be the magnitude of the magnetization isochromat in the (ijk) voxel. In a single iteration of the pulse sequence, the first inversion pulse will invert the magnetization according to some row, m, of an N_xth-order Hadamard matrix, in effect performing the transformation $M_{ijk} \rightarrow H_{mi} M_{ijk}$. The order of the matrix is omitted from the notation for clarity. The second and third inversion pulses will then invert the bands along the y and z, according to the nth and qth rows of an N_yth- and N_zth-order Hadamard matrix, respectively. At the end of the (mnq) iteration, the magnetization in the ijk voxel is:

$$M_{ijk}^{(mnq)} = H_{mi} H_{nj} H_{qk} M_{ijk} \quad [4]$$

The FID acquired by exciting the sample and acquiring is:

$$\mathrm{FID}^{(mnq)}(t) = \sum_{ijk} M_{ijk}^{(mnq)} e^{i\Omega_0 t} = \sum_{ijk} H_{mi} H_{nj} H_{qk} s_{ijk}^{(\mathrm{single})}(t) \quad [5]$$

where $s_{ijk}^{(\mathrm{single})}(t)$ is the signal originating solely from the ijk voxel, and the summation extends over all voxels. Acquiring all possible permutations of (mnq), the individual signals $s_{ijk}^{(\mathrm{single})}(t)$ can be recovered by performing an inverse Hadamard transform; that is, summing and subtracting the FIDs according to the rows of the Hadamard matrix:

$$\frac{1}{N_x N_y N_z} \sum_{m=1}^{N_x} \sum_{n=1}^{N_Y} \sum_{q=1}^{N_z} H_{mi} H_{nj} H_{kq} \mathrm{FID}^{(mnq)}(\mathrm{t}) = s_{ijk}^{(\mathrm{single})}(\mathrm{t}). \quad [6]$$

This identity is proven by substituting Eq. 5 into the right-hand side of Eq. 6 and applying Eq. 1 repeatedly, until $s_{ijk}^{(\mathrm{single})}(t)$ is recovered.

Outer Volume Considerations

The above discussion has not taken into account the contributions from volumes outside the VOI. Outer volumes can be broadly divided into three distinct groups: those that undergo two Hadamard inversions ($M_{jk}^{(yz)}$, $M_{ik}^{(xz)}$, $M_{ij}^{(xy)}$); those that undergo a single inversion ($M_i^{(x)}$, $M_j^{(y)}$, $M_k^{(z)}$); and those that are unaffected by any of the three Hadamard pulses, M_0. The superscripts indicate which of the three Hadamard pulses affect the magnetization, whereas the subscripts indicate the position of the volume, as illustrated in Fig. 1c. The effect of the three Hadamard pulses on each of these outer volumes during the (mnq) scan is:

$$\begin{array}{ll} M_0 & \rightarrow M_0 \\ M_i^{(x)}, M_j^{(y)}, M_k^{(z)} & \rightarrow H_{mi} M_i^{(x)}, H_{nj} M_j^{(y)}, H_{qk} M_k^{(z)} \\ M_{ij}^{(xy)}, M_{jk}^{(xz)}, M_{jk}^{(yz)} & \rightarrow H_{mi} H_{nj} M_{ij}^{(xy)}, H_{nj} H_{qk} M_{jk}^{(xz)}, H_{nj} H_{qk} M_{jk}^{(yz)}. \end{array} \quad [7]$$

These signal contributions must be summed over all indices and added to the FID (Eq. 5). After applying the

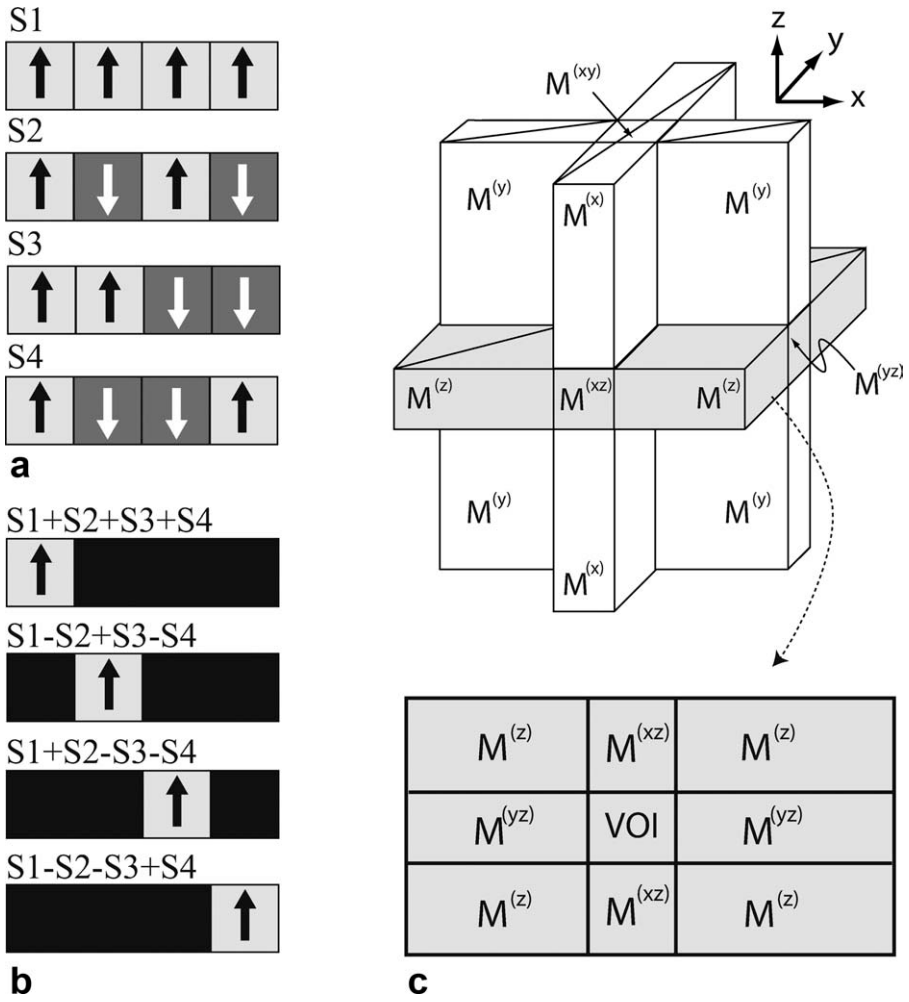

FIG. 1. Principles of Hadamard encoding. **a:** An example: 1D, fourth-order Hadamard encoding. Four scans are carried out, inverting the voxels $S_1,\ldots,S_4$, according to the rows of a 4 $\times$ 4 Hadamard matrix. This is followed by excitation and acquisition. **b:** By adding and subtracting the four scans, the signal from each of the voxels can be recovered. **c:** In a 3D protocol, three consecutive Hadamard pulses along orthogonal axes (x, y, z) are used to encode the spins. The sample can be partitioned into one of four regions: the VOI, which experiences all three pulses; spins that undergo two pulses ($M^{(xy)}$, $M^{(xz)}$, $M^{(yz)}$); spins that undergo a single pulse ($M^{(x)}$, $M^{(y)}$, $M^{(z)}$); and spins that do not experience any of the pulses (M_0). Top: the intersection of the planes in 3D. Bottom: a 2D view of the region inverted by the pulse along z, highlighted in gray.

inverse Hadamard transform (Eq. 6), one recovers not only the signal $s_{ijk}^{(\mathrm{single})}(t)$ from the (ijk)th voxel, but additional terms as well:

$$\begin{aligned}\frac{1}{N_xN_yN_z}\sum_{m=1}^{N_x}N_x\sum_{n=1}^{N_y}\sum_{q=1}^{N_z}H_{mi}H_{nj}H_{kq}\mathrm{FID}^{(mnq)}(\mathrm{t})\\ = s_{ijk}^{(\mathrm{single})}(t)\\ + \delta_{i1}M_{jk}^{(yz)} + \delta_{j1}M_{ik}^{(xz)} + \delta_{k1}M_{ij}^{(xy)}\\ + \delta_{i1}\delta_{j1}M_k^{(z)} + \delta_{i1}\delta_{k1}M_j^{(y)} + \delta_{j1}\delta_{k1}M_i^{(x)}\\ + \delta_{i1}\delta_{j1}\delta_{k1}M_0.\end{aligned} \quad [8]$$

The new terms represent outer volume contamination, which renders the exterior planes ($i = 1$, $j = 1$, $k = 1$) in the $N_x \times N_y \times N_z$ MRSI grid unusable, a known limitation of Hadamard Encoding (18).

Hadamard Pulse Synthesis

To spatially encode N voxels along a particular dimension, L-HSI inverts $N/2$ bands (corresponding to the $H_{ij} = -1$entries in the Hadamard matrix) using a multiband adiabatic RF pulse (25). Such a pulse, $B_1^{(\mathrm{multi})}(t)$, inverting $N/2$ bands having center frequencies at ω_k, $k = 1,\ldots, N/2$, can be constructed by summing up time and frequency shifted individual adiabatic inversions (25):

$$B_1^{(\mathrm{multi})}(t) = \sum_{k=1}^{N/2} B_1^{(\mathrm{single})}(t + (k-1)\tau)e^{i\omega_k t} \quad [9]$$

where $B_1^{(\mathrm{single})}$ is a single-band adiabatic inversion pulse having bandwidth and duration $T^{(\mathrm{single})}$. By choosing a long enough τ, the overlap between the individual pulses $B_1^{(\mathrm{single})}$ can be reduced to keep the train's peak power to approximately equal that of a single pulse, $B_1^{(\mathrm{single})}$. As opposed to merely superimposing the pulses, the train (Eq. 9) allows for an ($N/2$)-fold increase in the bandwidth per inversion band per given maximal B_1, and consequently for an ($N/2$)-fold increase in the spatial field gradients, reducing chemical shift and main field inhomogeneity artifacts.

It should be noted that, for a given Hadamard order, N, no bands are inverted on the first scan (as the $H_{1i} = 1$ for all i) and $N/2$ bands are inverted in the subsequent ($N - 1$) scans (as the number of entries $H_{ij} = -1$ for $i \neq 1$ is $N/2$). The duration of a pulse train (Eq. 9) containing $N/2$ summands and designed to invert $N/2$ bands is:

$$T_N^{(\max)} = T^{(\mathrm{single})} + \left(\frac{N}{2} - 1\right)\tau. \quad [10]$$

In those scans in which no bands are inverted, a delay given by Eq. 10 is introduced in place of the pulse train to eliminate T_1-induced signal variations between scans.

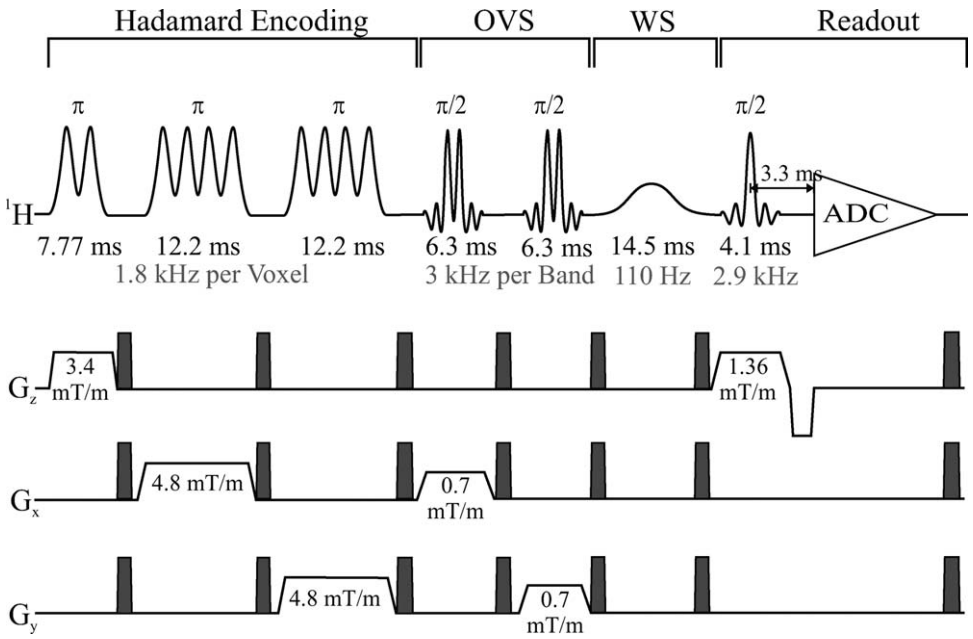

FIG. 2. The 3D L-HSI pulse sequence. Durations and gradients strengths are denoted for the in vivo MRSI experiment described in the text; spoiling gradients are highlighted in black. Pulse bandwidths are shown below the pulse durations in gray. A WET water suppression module, not shown, is executed just prior to the Hadamard-encoding block. For a volume containing $N_x \times N_y \times N_z$ voxels, the sequence is repeated $N_xN_yN_z$ times. Note the Hadamard pulse trains (Eq. 9) and the OVS longitudinal module, placed close to excitation for increased lipid suppression.

MATERIALS AND METHODS

All experiments were carried out on a 3 T full body imager (Siemens Magnetom Trio, Siemens AG, Erlangen, Germany). The manufacturer's provided ^{1}H 3 T quadrature transmit–receive head-coil was used. It was capable of delivering a 0.9 kHz (21.2 μT) B_1 with ~2 kW of RF power into a human head-size load.

Pulse Sequence

Unless otherwise specified, all pulses were calibrated to the available peak B_1 amplitude of 0.9 kHz (21.2 μT). The 3D L-HSI pulse sequence is shown in Fig. 2. The Hadamard encoding pulse trains all use $T^{(\text{single})} = 5.5$ ms, $\tau = 2.2$ ms (see Eq. 10), with $B^{(\text{single})}$ being a hyperbolic secant pulse with a bandwidth of 1.8 kHz (26). The Hadamard pulse trains are followed by an outer volume saturation module, comprised of two 6.3-ms long spatially selective dual-band π/2-pulses (3.0 kHz bandwidth for each band) along the read and phase axes, designed to excite and subsequently dephase the magnetization outside the VOI, and an additional low peak power, frequency selective 14.5 ms Gaussian CHESS pulse (110 Hz bandwidth) for added water suppression; finally, the axial slab containing the VOI is excited onto the transverse plane using a spatially selective 4.1 ms Shinnar-Le Roux designed π/2-pulse along the slice axis with a bandwidth of 2.9 kHz. Note that, as L-HSI encodes the spins' positions along the longitudinal axis, all magnetization must be dephased after each scan, necessitating the use of π/2 excitation pulse; as a result, optimal SNR is obtained by setting pulse repetition time (TR) $\approx 1.2T_1$, which, for most in vivo brain metabolites at 3 T, implies TR ≈ 1.5 s (27). A FID is acquired immediately following a refocusing gradient. We denote by TE* the acquisition delay, i.e., the time between the center of the selective excitation pulse and beginning of acquisition. In the current sequence, TE* was set to 3.3 ms.

Phantom

To validate the L-HSI protocol, a 1 × 1 × 4 MRSI experiment was performed on a 12 × 5 cm^2 (diameter × length) plastic cylinder comprised of four 1.25-cm partitions (including a 1-mm wall), immersed in a larger water-filled tube to reduce air–water susceptibility, as shown in Fig. 3. Each partition contained a different 100 mM (proton concentration) solute yielding a singlet at a distinct chemical shift: methanol (Meth), Na-acetate (NaAc), *tert*-buthanol (*t*-BU), and Na-3-methyl-silyl propionate (Na-3-Si) at 3.4, 2.2, 1.2, and 0.0 ppm, a similar range to that encountered in vivo. The sample, as well as the VOI, are shown in Fig. 3a, with the VOI taken to be 11 × 11 × 5 cm^3. After shimming the sample to a 6 ± 1 Hz linewidth, a 5:26 min 3D magnetization prepared rapid acquisition gradient echo (MPRAGE) with isotropic 1 mm^3 voxels (FOV 256 × 256 × 192 mm^3) was acquired for VOI placement. Following this, two sequences were executed back-to-back: 3D L-HSI and 3D CSI.

The Hadamard pulse train (Eq. 9, with 21.2 μT = 0.9 kHz peak B_1 and a bandwidth of 1.8 kHz per voxel) was executed in the presence of 3.4 mT/m gradients along the partitions' axis, resulting in a chemical shift displacement of 0.9 mm/ppm at 3 T. The total Hadamard encoding block, including all spoiler gradients, took 13 ms. TR was set to 1500 ms. A 1D inverse Hadamard transform was used along the three spatial axes to localize the signal. Note that the first voxel contains contamination from the water outside the VOI. However, as water suppression was applied and the chemical shifts of the observed peaks in each partition differed from that of water, the quantification of leakage and SNR were not affected. For 3D CSI, the manufacturer provided sequence was used, with STEAM (TE/mixing period (TM)/TR = 15/10/1500 ms) used to define the VOI. The slice selection pulse was matched to the slice-selective excitation pulse used in the L-HSI sequence (4.1 ms, 2.9 kHz bandwidth) and was executed in the presence of 1.4

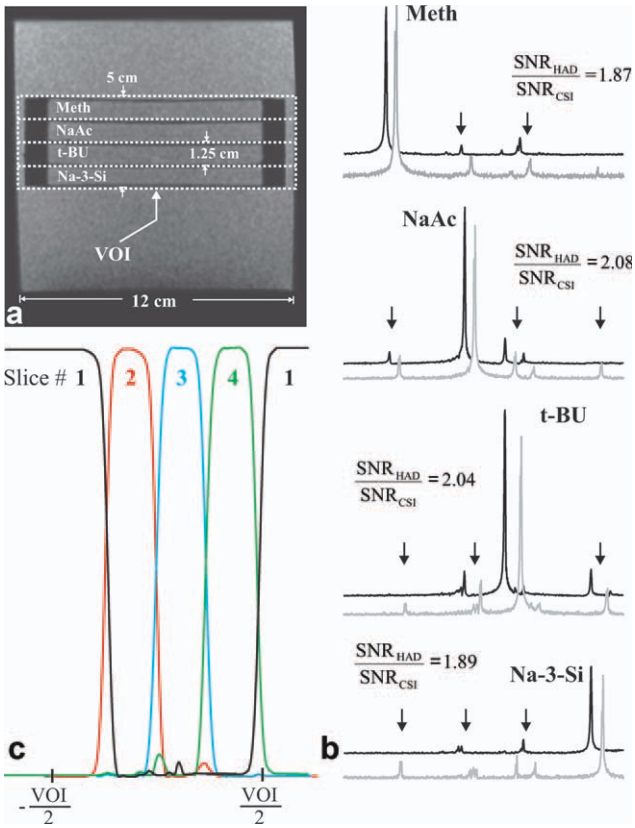

FIG. 3. Comparison between L-HSI and STEAM-CSI in a phantom. **a:** A sagittal image showing the placement of the VOI. Note that each L-HSI slice contains a single partition, having a single chemical species. **b:** The L-HSI (black) and STEAM-CSI (gray) spectra recovered from each voxel (different voxels are placed inside different partitions). The STEAM-CSI spectra were scaled to twice their height, to visually compensate for the factor of ½ loss in SNR inherent to STEAM. The SNRs (Hadamard vs. STEAM-CSI) are noted next to each partition's peak. Note the reduced voxel bleed (indicated by black arrows) in L-HSI, especially from noncontiguous voxels. **c:** Computer simulated voxel profiles for fourth-order Hadamard encoding, obtained by simulating the four Hadamard pulse trains, and then adding and subtracting the resulting frequency profiles to retrieve the voxel profiles. Note the outer volume contamination of voxel #1, and the absence of long-range "bleed" in other profiles (#2, #3, and #4), as evident by the profiles' decay to zero outside the voxels' boundaries.

mT/m gradients along the phantom's axis, resulting in a chemical shift displacement of 2.2 mm/ppm. The FOV was taken to coincide with the VOI ($11 \times 11 \times 5$ cm^3). A 3D inverse Fourier transform was used along the three spatial axes to localize the signal.

For both sequences, TR = 1.5 s and eight prescans were used to drive the magnetization to dynamic equilibrium; thus, each experiment lasted exactly 18 s. A 1024-point FID with a dwell time of 1 ms and filter bandwidth of ±500 Hz was acquired each scan, and subsequently zero-filled to 2048 points and Fourier transformed. Zeroth- and first-order phase corrections were carried out manually on the resulting four spectra.

To confirm the spatial localization of the L-HSI protocol along the phantom's axis, the spatial inversion profiles of each of the fourth-order Hadamard pulses was simulated by solving the Bloch equation numerically in the presence of relaxation (T_1 = 1 s, T_2 = 0.1 s), for a 4-cm homogeneous sample having no chemical shift. The inversion profiles were inverse-Hadamard transformed, by adding and subtracting them according to Eq. 6, to recover the voxel profiles. The simulation's parameters matched those used in the phantom experiment.

Human Subject

A normal healthy volunteer (male, age 29) was studied after written institutional review board-approved consent was obtained. For VOI placement an axial 3D MPRAGE was acquired in 5:26 min, with a $1 \times 1 \times 1$ mm^3 resolution and a $256 \times 256 \times 192$ mm^3 FOV. The whole brain was then shimmed using an in-house 3D CSI-based autoshimming technique down to 25 Hz (full width at half maximum), respectively. The fully automated procedure takes ~1 min per iteration and requires between 2 and 4 iterations to achieve this linewidth (28). Following shimming, a 3D L-HSI dataset was acquired. The entire protocol took just under 40 min.

The 3D L-HSI sequence timing and gradients are shown in Fig. 2. For all pulses, the transmitter was centered on the N-acetyl aspartate (NAA) singlet at 2 ppm. The overall duration of the Hadamard encoding block was 38 ms, with chemical shift displacements equal to 0.6 mm/ppm along the in-planes (x and y) axes and 0.9 mm/ppm along the slice-selective (z) axis. The OVS module lasted 19 ms. A TE* = 3.3 ms delay was introduced between the middle of the excitation pulse and acquisition to allow for a gradient refocusing lobe, after which a 512-point FID was acquired, with a dwell time of 0.5 ms and a ±1 kHz bandwidth. Spoiler gradients (15 mT/m) were applied following each acquisition to spoil the transverse magnetization in preparation for the following scan. The VOI was $7 \times 7 \times 5$ cm^3 large and consisted of $8 \times 8 \times 4$ voxels (0.96 cm^3) along the x, y, and z axes, respectively. At TR = 1.5 s and four averages ($4 \times 8 \times 8 \times 4 = 1024$ scans), the in vivo MRSI took 26 min.

The entire protocol was repeated five times on four consecutive days with identical parameters (up to slight unavoidable variations in shimming and VOI placement) to test for robustness and reproducibility. The same volunteer was used for all scans to eliminate intersubject variability. To assess overall robustness, the NAA peak's full width at half maximum was quantified for all voxels for which its peak height exceeded 50% of its maximal value (maximized over all voxels for that particular scan).

Postprocessing

To correct for B_0 drift, a whole-head FID was acquired before each average and at the conclusion of the experiment for a total of 5 FIDs, and the position of the water peak was noted. The drift was found to be linear to a good approximation with a rate $\alpha_{drift} = 13$ Hz/h.

The acquired 3D L-HSI encoded ^{1}H-MRSI data was processed using in-house software written in MATLAB 2009b (Mathworks, Natick, MA). Each FID was zero-filled to 1024 points, and B_0 drift-correction was applied

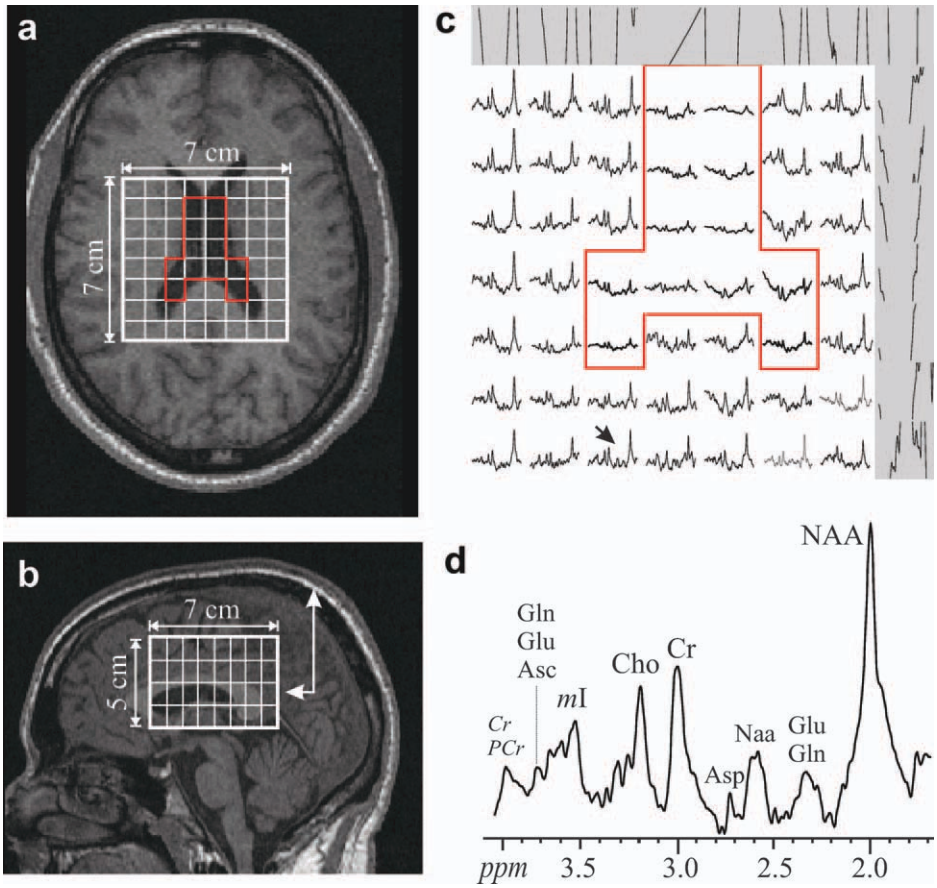

FIG. 4. In vivo 3D L-HSI spectra obtained from an 8 × 8 × 4 cm^3 spectroscopic grid (voxel size 1 × 1 × 1 cm^3) in a human volunteer. **a,b:** VOI placement and dimensions on axial (top) and sagittal (bottom) T_1 weighted images. The axial slice shown in (a) is marked with a white arrow on the sagittal image in (b). **c:** Spectra from the topmost 8 × 8 spectroscopic slice. Note the contaminated voxels in the outer planes (highlighted in gray). **d:** An expanded spectrum from a single voxel, noted with a black arrow in (c). Note the short TE* = 3.3 ms features such as the *myo*-inositol (*m*I) at about 3.55 ppm, glutamate/glutamine around 2.3–2.4 ppm, and creatine's methylene peak around 3.9 ppm. The ppm axis also serves as a zero line for the data. [Color figure can be viewed in the online issue, which is available at wileyonlinelibrary.com.]

by multiplying each FID by a linear phase, $e^{i(\alpha_{drift}\tau_i)t}$, where τ_i is the time of acquisition of the ith FID (τ_i = 0, 1.5 s, 3 s, 4.5 s, …), and t is the acquisition time during the scan (t = 0, 0.5 ms, 1 ms, …). The linear phase shift $\phi(v) = v \times$ TE* accrued because of the nonzero acquisition delay (TE*) was removed by multiplying all spectra by $e^{-i\phi(v)}$. The FIDs were then Fourier transformed along the time axis, and Hadamard (for L-HSI) or Fourier (for CSI) transformed along the three spatial axes. Finally, automatic zeroth- and first-order phase corrections were applied.

RESULTS

Phantom

The spectra reconstructed from each of the four partitions are shown in Fig. 3b for both CSI and L-HSI. The CSI spectra were scaled to twice their height, as the STEAM-based localization halves the SNR. L-HSI is expected to yield an improvement in SNR of a factor slightly greater than 2 compared to STEAM-CSI, due to the inherent signal loss of STEAM and the reduced voxel bleed from each voxel in L-HSI. The SNR between L-HSI and CSI, quantified for each spectrum, is noted in Fig. 3b. Not quite the full expected increase was observed in all partition, and we attribute this to ambiguities associated with the placement of the VOI. These deviations are of the order of several percent, corresponding to shifts of fractions of a millimeter, a resolution unavailable with the 3D MPRAGE used for VOI placement. This issue affects the VOI placement in both L-HSI and CSI and, consequently, the quantification in the first and last compartments (i.e., only those compartments at the edges of the VOI slice-selective pulse). An additional source of discrepancy between the measured and predicted SNRs could be relaxation losses induced during the Hadamard encoding module. Nevertheless, the measurement confirms, to within several percent, the SNR gains expected with L-HSI.

In most spectra, more signal bleed between voxels (as manifested by peaks belonging to metabolites from extraneous partitions) is observed for CSI than L-HSI. In several of the spectra, CSI shows bleed from nonadjacent partitions as well. However, L-HSI shows such bleed as well in the methanol spectrum. This may be the result of imperfections in the PSFs, chemical shift displacements associated with the Hadamard RF pulses, or localization-related "ISIS-like" T_1-smearing effects due to the TR/T_1 ratio being on the order of unity (29,30).

Human Subject

Figure 4 shows the spectra acquired from one of the four axial 8 × 8 spectroscopic slices going through the ventricles using 3D L-HSI from the first scan (out of five). Extraneous contamination can be observed in the 15 voxels belonging to the outer planes (left-most column and top-most row in Fig. 4c), as discussed in the theory section. The ventricles, outlined on the MPRAGE's axial

slice with a red line (Fig. 4a), are also outlined in the set of spectra (Fig. 4c) and show reduced signal, demonstrating the localization of the PSF. An enlarged spectrum from one of the voxels, indicated by an arrow in Fig. 4c, is shown in Fig. 4d, showing short TE* features such as the *myo*-inositol (*m*I) at about 3.55 ppm, glutamate/glutamine around 2.3–2.4 ppm and the creatine methylene peak around 3.9 ppm. The full width at half maximum linewidth of the NAA averaged over all voxels for the particular scan shown was 7 ± 2 Hz (mean ± standard deviation). SNR was quantified using the NAA peak and the noise's standard deviation in the 10–12 ppm range in 10 voxels containing mostly white matter and found to be 32 ± 9 (mean ± standard deviation). Rolling baseline artifacts were minimal in the shown spectral range, even after the first-order phase correction was applied to correct for the 3.3 ms TE*. Similar quality spectra were obtained for all five scans on the same volunteer. To quantify the reproducibility, the NAA peak's full width at half maximum was averaged over all scans and all voxels that met the inclusion criteria (i.e., NAA peak height at least 50% of its maximal value) was 7 ± 3 Hz.

DISCUSSION

Longitudinal Hadamard encoding has been reported previously in the literature for phantoms (15,18,31). In vivo results have been confined to 31P in the muscle (32,33). In these studies, the absence of the large water and fat resonances outside the VOI made OVS modules redundant. This article presents an implementation of full 3D L-HSI on a clinical scanner in the human brain, capable of significant coverage while offering good water suppression and rejection of outer volume contamination, as well as direct observation of an FID with minimal (approximately a few ms) acquisition delay, thus also facilitating the study of short T_2 and J-coupled metabolites.

Conventional, Fourier-encoded 3D multivoxel MRSI uses the same gradient phase encoding principles so well known from MRI. Its most attractive advantages include low SAR (no RF needed for encoding), modularity, and simplicity. However, this encoding paradigm is not well suited for the relatively coarse resolution used in MRSI, due to its significant intervoxel bleed at low resolutions. Replacing the Fourier phase-encoding module with a Hadamard one alleviates concurrently several of the problems associated with CSI: (i) it minimizes intervoxel leakage and nearly eliminates long range bleed; (ii) it offers inherent suppression of signals from outside the VOI, relaxing requirements on OVS modules. These OVS modules can then be made longitudinal—i.e., made to excite and dephase the lipid signals while the metabolites' spins are stored along the longitudinal axis—and placed in proximity to the excitation to minimize the recovery of the fat and water signals from outside the VOI; and (iii) the removal of echo-based localization modules, such as PRESS and STEAM, allows for the acquisition of non-spin-echo spectra, minimizing both T_2 losses and J-coupling modulation; (iv) the highly localized PSF and decreased signal leakage result in a greater SNR and improved localization; (v) the voxels do not need to be contiguous; (vi) as each slice is inverted individually, high-bandwidth pulses can be used for encoding irrespective of the VOI size, thereby reducing chemical shift displacements; (vii) the adiabatic inversion RF pulses used "lock" the spins, which prolongs the relaxation times and minimizes J-coupled evolution, as they cross the transverse plane. Furthermore, the adiabatic pulses used in L-HSI make it translatable to surface coils or to high fields, where B_{1+} inhomogeneities are pronounced. Also noteworthy is that fact that voxel shifting, previously thought to be only applicable to CSI, has also been recently implemented for Hadamard-encoded data sets (34).

L-HSI's localization is obtained by RF irradiation. This bears semblance to ISIS (35), where a volume is selected by playing out three orthogonal RF pulses and adding/subtracting eight scans, and can be considered its multivoxel extension. The use of RF pulses for localization presents several challenges not found in CSI: (i) To avoid chemical shift displacements, strong gradients must be used; however, the voxels' bandwidths are limited by the RF's peak power, which diminishes at higher B_0, reducing the effectiveness of the method at ultrahigh fields. In this study, the displacements encountered in vivo ranged from 0.6 to 0.9 ppm/mm. (ii) A related issue is that of the Hadamard pulses' associated SAR, which tends to limit the duty cycle and TR. In the in vivo MRSI sequence presented, SAR levels were at 76% of the allowed maximum with a TR of 1.5 s. (iii) The voxels' spatial profiles are not entirely orthogonal: the finite RF durations result in transition bands in their corresponding spatial profiles. These are ultimately perceived as a nonzero bleed. However, in contrast to CSI, this bleed can be made arbitrarily small, by shrinking the voxel profiles (albeit at some cost to SNR); in addition, it is almost entirely from regions in the immediate vicinity of the voxel, as shown in Fig. 3c. (iv) Any imperfections in the RF transmitter affect the voxel profiles directly. (v) Although OVS is inherent to the Hadamard-encoding scheme, some form of suppression module is still needed to suppress the intense lipid signals from outside the VOI. However, as L-HSI encodes the spins' positions longitudinally, the suppression module can also be made longitudinal, with minimal losses to the metabolites' signals due to their long T_1s. (vi) Hadamard encoding renders three planes unusable due to outer volume contamination, as observed in Fig. 4c. (vii) As RF-encoding encodes the spins' positions in physical space, patient motion might lead to mislabeling of these positions and, consequently, to localization errors. In this study, the patient's head was held in place during the scan. However, to fully compensate for such errors, the motion should be tracked and the RF pulses should be adjusted in real time, using, e.g., navigator echoes (36). (viii) Much like ISIS, L-HSI is prone to so-called "T_1-smearing" effects if TR is short compared to T_1 and the magnetization is not fully excited and spoiled after each scan (29,30). If not addressed, either by taking TR $> T_1$ or by using adiabatic excitations, these can lead to localization errors that can offset the PSF advantages offered by L-HSI. Both the phantom and the in vivo results shown herein (Figs. 3 and 4) display good

localization and suggest that this may not be a major issue with L-HSI.

L-HSI and Short Echo Time Spectroscopy

The complexity of short echo time spectra and presence of an extreme macromolecular baseline are often offset by the prospects of simultaneously observing several important short-lived resonances, such as glutamate and gamma-aminobutyric acid (GABA). The acquisition of such spectra has, therefore, become a lively area of research. Several approaches to short-TE spectroscopy have been suggested. These can be partitioned into methods that try to minimize the duration of the OVS module and try to do away with it. In the first category, short echo time STEAM sequences with TEs as short as 4 ms at 4 T and 6 ms at 7 T have been reported (37). To achieve such short echo times, however, very short volume selection pulses must be used, leading to wide transition bands and poor VOI definition. Another approach that is often combined with stimulated echo acquisition, echo planar spectroscopic imaging, often features short echo times, with reports of echo times as short as 5 ms in the literature (38) (albeit at a lower 1.5 T). Localization by adiabatic selective refocusing (LASER)-based localization (39) and its semi-LASER variant, using six or four consecutive adiabatic full passages, can achieve fairly short TEs, and recent reports of TE = 30 have been made (40,41) despite the often long pulse durations associated with adiabatic pulses. For pulse spacing that is short compared to the reciprocal of the J-coupling and the spread in chemical shifts, J-coupling effects can be neglected (42), minimizing their losses despite the 30 ms echo time.

The second category, to which L-HSI belongs, is usually comprised of preparation modules designed to null intense extraneous lipid signals, followed an acquisition of an FID. FIDLOVS (43) is one such approach, with a reported TE* of 5.6 ms at 7 T; Bogner et al. (44) have carried out high resolution with an ultrashort TE* of 1.3 ms. The main advantages of such approaches are the minimization of J-coupling signal losses and an increase in the SNR, especially at high fields (7 T) where T_2 relaxation times dip below 100 ms (45) and T_2-weighting can become significant. In contrast, the long, 1–1.5 s T_1s available in vivo at even 3 T (46,47) make longitudinal encoding and OVS modules appealing.

As with all FID-based sequences, first-order phasing can turn out to be an issue if too long an acquisition delay (TE*) is used. Modern fitting software can often take this into account by fitting the spectrum to basis functions simulated with the appropriate TE* (48). Furthermore, when comparing FID-based to spin-echo-based sequences, one must keep in mind that the acquisition delay introduces a signal attenuation given by $\exp(-TE^*/T_2^*)$, while an echo only attenuates the signal by a smaller amount, $\exp(-TE/T_2)$; thus, for a given TE = TE*, an echo-based sequence will theoretically yield better SNR than an acquisition-delay based one. However, as the acquisition delays often used in FID-based sequences are so short ($TE^* \ll T_2^*$), this difference is entirely negligible.

It should be noted that any increase in the SNR per unit time of L-HSI over spin-echo-based spectroscopic approaches (e.g., PRESS and LASER) comes solely from its RF-encoded PSF, assuming $TE = TE^* \ll T_2^*$. The improvements in the PSF are independent of L-HSI's inherent outer volume rejection and its ability to acquire short echo time spectra; indeed, it is possible, if so desired, to combine longitudinal HSI encoding with an additional subsequent echo-based OVS module. In that way, the advantages associated with its RF-encoded PSF can be augmented by, say, a PRESS or LASER (39) volume selection, when the VOI must be placed close to sources of intense lipid signals and the dual-pulse approach suggested in this article is insufficient (e.g., the prostate, or very close to the skull).

We conclude by noting a third, "hybrid" category for short-TE sequences could be introduced, consisting of pulse sequences that combine echo-based and longitudinal methods. This category includes the SPECIAL approach, which combines longitudinal and transverse localization, and has recently reported clinical TEs as short as 3.5 ms at 3T (49,50), as well as various implementations combining Hadamard encoding with Fourier encoding, with reported TEs of 35 ms (17). Such hybrid approaches enjoy the advantages and disadvantages offered by both approaches and can be used to reduce the echo time while still enjoying some of the advantages of echo-based modules (e.g., phased spectra).

CONCLUSIONS

L-HSI enables the acquisition of non-spin-echo 3D multivoxel spectra, with RF (rather than gradient phase) encoding. Consequently, it introduces a very short (~4 ms) delay between the excitation of the spins onto the transverse plane and acquisition. The short delay is advantageous in reducing T_2 weighting of the spectra and J-coupling modulation artifacts. In addition, it offers an inherently superior PSF, yielding less contamination from outer-volume signals and reduced cross-voxel bleed whenever a small number of voxels ($N = 2, 4, 8$) is involved. As multivoxel spectroscopy is often carried out at such low resolutions, L-HSI presents an alternative to the more traditional Fourier-based methods. Implementation of 3D proton L-HSI on a commercial clinical imager is straightforward, consisting of three one-dimensional adiabatic inversion pulses, readily executable using any modern RF pulse synthesizer.

ACKNOWLEDGMENTS

Assaf Tal acknowledges the support of the Human Frontiers Science Project.

REFERENCES

1. Mountford CE, Stanwell P, Lin A, Ramadan S, Ross B. Neurospectroscopy: the past, present and future. Chem Rev 2010;110:3060–3086.
2. Zhu H, Barker PB. MR spectroscopy and spectroscopic imaging of the brain. In: Modo M, Bulte JWM, editors. Magnetic resonance neuroimaging, Vol. 711. Springer-Verlag, Berlin, Germany; 2011. pp 203–226.
3. Horska A, Barker PB. Imaging of brain tumors: MR spectroscopy and metabolic imaging. Neuroimaging Clin N Am 2010;20:293–310.
4. Graaf Mvd. In vivo magnetic resonance spectroscopy: basic methodology and clinical applications. Eur Biophys J 2010;39:527–540.
5. Maudsley AA, Hilal SK, Perman WH, Simon HE. Spatially resolved high resolution spectroscopy by "four-dimensional" NMR. J Magn Reson 1983;51:147–152.

6. Brown TR, Kincaid BM, Ugurbil K. NMR chemical shift imaging in three dimensions. Proc Natl Acad Sci USA 1982;79:3523–3526.
7. Maudsley AA. Sensitivity in Fourier imaging. J Magn Reson 1986;68: 363–366.
8. Wang Z, Bolinger L, Subramanian VH, Leigh JS. Errors of Fourier chemical-shift imaging and their corrections. J Magn Reson 1991;92:64–72.
9. Mareci TH, Brooker HR. Essential considerations for spectral localization using indirect gradient encoding of spatial information. J Magn Reson 1991;92:229–246.
10. Koch T, Brix G, Lorenz WJ. Theoretical description, measurement, and correction of localization errors in 31P chemical-shift imaging. J Magn Reson B 1994;104:199–211.
11. Parker DL, Gullberg GT, Frederick PR. Gibbs artifact removal in magnetic resonance imaging. Med Phys 1987;14:640–645.
12. Adalsteinsson E, Star-Lack J, Meyer CH, Spielman DM. Reduced spatial side lobes in chemical-shift imaging. Magn Reson Med 1999;42:314–323.
13. Frahm J, Merboldt KD, Hanicke W. Localized proton spectroscopy using stimulated echoes. J Magn Reson 1987;72:502–508.
14. Bottomley PA. Selective volume method for performing localized NMR spectroscopy. US Pat. 4,480,228, 1984.
15. Bolinger L, Leigh JS. Hadamard spectroscopic imaging (HSI) for multivolume localization. J Magn Reson 1988;80:162–167.
16. Gonen O, Murdoch JB, Stoyanova R, Goelman G. 3D multivoxel proton spectroscopy of human brain using a hybrid of 8th-order hadamard encoding with 2D chemical shift imaging. Magn Reson Med 1998;39:34–40.
17. Gonen O, Arias-Mendoza F, Goelman G. 3D localized in-vivo 1H spectroscopy of human brain by using a hybrid of 1D-Hadamard with 2D-chemical shift imaging. Magn Reson Med 1997;37:644–650.
18. Goelman G, Leigh JS. B_1-insensitive Hadamard spectroscopic imaging technique. J Magn Reson 1991;91:93–101.
19. Lei H, Peeling J. Multiple-voxel double-quantum lactate-edited spectroscopy using two-dimensional longitudinal Hadamard encoding. Magn Reson Med 1999;42:19–23.
20. Kupce E, Freeman R. Frequency-domain Hadamard spectroscopy. J Magn Reson 2003;162:158–165.
21. Tal A, Shapira B, Frydman L. Single-scan 2D Hadamard NMR spectroscopy. Angew Chem 2009;121:2770–2774.
22. Sloane NJA. Fourier, Hadamard and Hilbert transforms in chemistry. In: Marshall AG, editor. Hadamard and other discrete transforms in spectroscopy. Plenum Publishing, New York; 1982. pp 45–67.
23. Gonen O, Hu J, Stoyanova R, Leigh JS, Goelman G, Brown TR. Hybrid Three dimensional (1D-Hadamard, 2D-chemical shift imaging) phosphorus localized spectroscopy of phantom and human brain. Magn Reson Med 1995;33:300–308.
24. Ryser HJ. Combinatorial mathematics. John Wiley and Sons, New York; 1963.
25. Goelman G. Two methods for peak RF power minimization of multiple inversion-band pulses. Magn Reson Med 1997;37:658–665.
26. Silver MS, Joseph RI, Hoult DI. Selective spin inversion in nuclear magnetic resonance and coherent optics through an exact solution of the Bloch-Riccati equation. Phys Rev A 1985;31:2753–2755.
27. Gonen O, Mohebbi A, Stoyanova R, Brown TR. In vivo phosphorous polarization transfer and decoupling from protons in three-dimensional localized nuclear magnetic resonance spectroscopy of human brain. Magn Reson Med 1997;37:301–306.
28. Hu J, Javaid T, Arias-Mendoza F, Liu Z, McNamara R, Brown TR. A fast, reliable, automatic shimming procedure using 1H chemical-shift-imaging spectroscopy. J Magn Reson B 1995;108:213–219.
29. Lawry TJ. Computer simulations of MRS localization techniques: an analysis of ISIS. Magn Reson Med 1989;9:299–314.
30. Burger C, Buchil R, Mckinnon G, Meier D, Boesiger P. The impact of the ISIS experiment order on spatial contamination. Magn Reson Med 1992;26:218–230.
31. Goelman G, Leigh JS. Hadamard spectroscopic imaging technique insensitive to pulse imperfections. J Magn Reson A 1993;105:78–81.
32. Goelman G. Fast Hadamard spectroscopic imaging techniques. J Magn Reson B 1994;104:212–218.
33. Goelman G, Glenn W, Leigh JS. Hadamard spectroscopic imaging technique as applied to study human calf muscles. Magn Reson Med 1992;25:349–354.
34. Fleysher L, Fleysher R, Liu S, Gonen O. Voxel-shift intepolation for Hadamard encoded MR images. Magn Reson Med 2008;60:524–535.
35. Ordidge RJ, Connelly A, Lohman JAB. Image-selected in-vivo spectroscopy (ISIS). A new technique for spatially selective NMR spectroscopy. J Magn Reson 1986;66:283–294.
36. Kozerke S, Schar M, Lamb HJ, Boesiger P. Volume tracking cardiac 31P spectroscopy. Magn Reson Med 2002;48:380–384.
37. Tkac I, Oz G, Adriany G, Ugurbil K, Gruetter R. In vivo 1H NMR spectroscopy of the human brain at high magnetic fields: metabolite quantification at 4 T vs. 7 T. Magn Reson Med 2009;62:868–879.
38. Seeger U, Klose U, Seitz D, Nagele T, Lutz O, Grodd W. Proton spectroscopy of human brain with very short echo time using high gradient amplitudes. Magn Reson Imaging 1998;16:55–62.
39. Garwood M, DelaBarre L. The return of the frequency sweep: designing adiabatic pulses for contemporary NMR. J Magn Reson 2001;153: 155–177.
40. Wijnen JP, van Asten JJA, Klomp DWJ, Sjobakk TE, Gribbestad IS, Scheenen TWJ, Heerschap A. Short echo time 1H MRSI of the human brain at 3T with adiabatic slice-selective refocusing pulses; reproducibility and variance in a dual center setting. J Magn Reson Imaging 2010;31:67–70.
41. Scheenen TWJ, Klomp DWJ, Wijnen JP, Heerschap A. Short echo time 1H-MRSI of the human brain at 3T with minimal chemical shift displacement errors using adiabatic refocusing pulses. Magn Reson Med 2008;59:1–6.
42. Allerhand A. Analysis of Carr-Purcell spin-echo NMR experiments on multiple-spin systems. I. The effect of homonuclear coupling. J Chem Phys 1966;44:1–9.
43. Henning A, Fuchs A, Murdoch JB, Boesiger P. Slice-selective FID acquisition, localized by outer volume suppression (FIDLOVS) for 1H-MRSI of the human brain at 7 T with minimal signal loss. NMR Biomed 2009;22:683–696.
44. Bogner W, Gruber S, Trattnig S, Chmelik M. High-resolution mapping of human brain metabolites by free induction decay 1H MRSI at 7 T. NMR Biomed (in press).
45. Marjanska M, Auerbach EJ, Valabregue R, van De Moortele P-F, Adriany G, Garwood M. Localized 1H NMR spectroscopy in different regions of human brain in vivo at 7 T: T2 relaxation times and concentrations of cerebral metabolites. NMR Biomed 2011;25: 332–339.
46. Traber F, Block W, Lamerichs R, Gieseke J, Schild HH. 1H metabolite relaxation times at 3.0 tesla: measurements of T_1 and T_2 values in normal brain and determination of regional differences in transverse relaxation. J Magn Reson Imaging 2004;19:537–545.
47. Mlynarik V, Gruber S, Moser E. Proton T_1 and T_2 relaxation times of human brain metabolites at 3 Tesla. NMR Biomed 2001;14: 325–331.
48. Soher BJ, Young K, Govindaraju V, Maudsley AA. Automated spectral analysis III: application to in vivo proton MR spectroscopy and spectroscopic imaging. Magn Reson Med 1998;40:822–831.
49. Mlynarik V, Gambarota G, Frenkel H, Gruetter R. Localized short-echo-time proton MR spectroscopy with full signal-intensity acquisition. Magn Reson Med 2006;56:965–970.
50. Mekle R, Mlynarik V, Gambarota G, Hergt M, Krueger G, Gruetter R. MR spectroscopy of the human brain with enhanced signal intensity at ultrashort echo times on a clinical platform at 3T and 7T. Magn Reson Med 2009;61:1279–1285.